Journal of
Manufacturing and Materials Processing

MDPI

Article

Microstructure Characterisation and Modelling of Pre-Forging Solution Treatment of 7075 Aluminium Alloy Using Novel Heating Methods

Hao Wu [1], Zisong Lu [2], Steven Hill [3] and Richard Turner [2,*]

[1] Dyson School of Design Engineering, Imperial College London, London SW7 2DB, UK; h.wu@imperial.ac.uk
[2] School of Metallurgy and Materials, University of Birmingham, Birmingham B15 2TT, UK; zlu98@outlook.com
[3] W.H. Tildesley Ltd., Willenhall WV13 2AN, UK
* Correspondence: r.p.turner@bham.ac.uk

Abstract: This study evaluates the effectiveness of these conventional heating methods, commonly adopted in the industry with long durations (typically one hour), in comparison to newer, potentially more efficient approaches such as induction coil heating, infrared module heating, and infrared furnaces that can perform solution heat treatment in significantly shorter times (5 to 20 min). The properties of the edge and centre regions of the solution-treated billets, including the state of precipitates, grain structures, and Vickers hardness, are investigated and compared. Results have shown that the 7075 billets heated by conventional heating methods sufficiently dissolved the stable precipitates, achieving hardness ranging from 137 to 141 HV, in contrast to the benchmark unheated, as-received sample of approximately 70 HV. In the meantime, the induction coil and infrared furnace demonstrate notable effectiveness, achieving hardness between 126 and 135 HV. The average grain sizes in the centre and edge regions for all samples are measured as 3 and 8 μm, respectively. However, the impact of the grain size on the hardness is negligible compared to the impact of the precipitates. Finite element (FE) modelling comparing the slowest heating method—the electric furnace—and the fastest heating method—induction coil heating—reveals the latter could heat the billet up to 450 °C at a rate ten times faster than the electric furnace. This study highlights the potential of novel heating techniques in promoting the efficiency of heat treatment processes for 7075 aluminium alloys.

Keywords: 7075 alloys; solution heat treatment; microstructure; finite element modelling

Academic Editor: Prashanth Konda Gokuldoss

Received: 18 November 2024
Revised: 7 December 2024
Accepted: 24 December 2024
Published: 25 December 2024

Citation: Wu, H.; Lu, Z.; Hill, S.; Turner, R. Microstructure Characterisation and Modelling of Pre-Forging Solution Treatment of 7075 Aluminium Alloy Using Novel Heating Methods. *J. Manuf. Mater. Process.* **2025**, *9*, 2. https://doi.org/10.3390/jmmp9010002

1. Introduction

Aluminium alloys are among the most extensively used materials for lightweight applications across various industries, including aerospace and automotive. Wrought aluminium alloys account for 80% of aluminium alloy production due to their excellent strength-to-weight ratio and superior mechanical properties, which can be significantly enhanced through work hardening and heat treatments [1].

The 7075 aluminium alloy, part of the 7xxx series (Al-Zn-Mg-Cu), is a precipitation-hardenable alloy renowned for its exceptional strength. A supersaturated solid solution (SSSS) is achieved through solution treatment at elevated temperatures, followed by rapid cooling to retain the dissolved alloying elements in an unstable state. Upon subsequent artificial ageing, a sequence of fine precipitates forms, progressively strengthening the alloy. In the early stages of precipitation hardening, Guinier–Preston (GP) zones form within the matrix as Zn and Mg atoms cluster into coherent or partially coherent Zn- and Mg-rich GPI

and GPII zones [2]. These GP zones serve as precursors to the metastable η′ phase, which typically has an average size in the nanometre range (~10–20 nm) and is semi-coherent with the aluminium matrix. The η′ phase is the primary strengthening phase, significantly contributing to their enhanced mechanical properties. As ageing progresses, the metastable η′ phase transforms into the stable η phase, which is larger (~20–50 nm) and incoherent with the matrix. This transformation reduces the material's strengthening effect, as the η phase interacts less effectively with dislocations, providing little resistance to plastic deformation [3–5].

The precipitate state in 7075 aluminium alloy is highly sensitive to temperature, soaking time, and heating/cooling rates, with significant changes occurring within the first few seconds/minutes of treatment. Precise control over these parameters is essential to achieve the desired size, distribution, and volume fraction of strengthening phases, such as GP zones and η′/η precipitates, as these microstructural characteristics directly determine the alloy's mechanical performance, such as hardness and tensile properties [2,5,6].

Forging is a crucial preliminary step for aluminium alloys, preparing the material for subsequent mechanical processing and heat treatments. In the case of 7xxx series alloys, an effective solution heat treatment is often essential prior to forging, as it enhances ductility and workability by dissolving alloying elements into SSSS, thereby obtaining a softened state of the alloy. This softened condition reduces the risk of cracks or defects, enabling smoother deformation during forging. Conventional heating methods for solution treatment, such as electric and gas furnaces, typically require preheating and extended soaking times, often lasting several hours, making the process inefficient and both costly and energy-intensive. This approach conflicts with current trends toward sustainable manufacturing, highlighting the need for alternative methods that offer greater energy and cost savings.

Efforts to date have focused on exploring new methods for solution treatment and refining the process for optimal efficiency. Chang et al. [7] investigated the effects of an infrared furnace compared to a conventional resistance furnace for solution heat treating 7075 aluminium alloy, using a 1-h solution treatment followed by artificial ageing at different temperature levels for 24 h. The results demonstrated an improvement in hardness of up to 10 HV with infrared heating when aged at 200 °C. Chayong et al. [8] explored a multistep induction heating approach prior to thixoforming 7075 alloys, demonstrating that induction heating facilitated recrystallisation within the alloy, and they recommended a hold time of 1 min or less at the solution temperature (475 °C) or at higher temperatures.

Huo et al. [9] examined the influence of heating rate during solution treatment on the microstructure and emerging mechanical properties of AA7075. They found that at rapid heating rates, the number of recrystallisation nucleation sites increases, leading to a fine, equiaxed grain structure. In contrast, slower heating rates result in coarser, elongated grains. Rometsch et al. [10] discussed advancements in retrogression heat treatments for several 7xxx series Al alloys, including 7075. They showed that with relatively small changes in retrogression heating re-ageing temperature, significant variations to the measured Vickers hardness could be achieved, with consequent variation to the formability and stress corrosion cracking performance.

Liu et al. [11] studied the properties of 2 mm thick 7075 sheets under various solution treatment conditions prior to T6 treatment. They reported that, with a constant soaking time of 30 min, increasing the temperature from 430 °C to 510 °C resulted in an increase in the hardness of 10 HV and a decrease in constituent particles from 4.29% to 2.38%. At the same solution temperature of 510 °C, extending the soaking time from 10 to 70 min led to a slight decrease in hardness (from 90 HV to 89.3 HV) and a reduction in constituent particles (from 3.21% to 2.05%). They also noted a minor increase in grain size associated with

longer soaking times. Similarly, Lee et al. [12] investigated solution treatment of 2.5 mm 7075 sheets, focusing on different solution temperatures (with a constant soaking time of 1 h) ranging from 400 °C to 500 °C. They found that after solution treatment, the hardness at 400 °C was approximately 80 HV, peaking at 475 °C with 88.9 HV. Additionally, after 24 h of natural ageing, there was an average hardness increase of around 30 HV across all solution temperatures.

Finite element (FE) modelling can be a useful tool for predictions of manufacturing outputs that are difficult to measure experimentally. Wu [13] used finite element simulation to study the thermal process of friction stir welding in 7050 alloys, showing that the peak temperature at the weld centre reached approximately 500 °C, leading to the dissolution of second-phase precipitates in the area within a relatively short welding cycle of less than 1 min. Zhang et al. [14] studied the impact of different heat treatments on the machinability and chip formation of 7075. Using experimental and FE modelling methods, they demonstrated that cutting forces for heat-treated 7075 vary, with the T6 condition exhibiting higher cutting forces than the retrogressed re-aged condition. Thus, heat treatments can be a significant influence on subsequent manufacturability.

Heat treatment accounts for up to 20% of the total energy cost in aluminium manufacturing [15]. With the increasing demand for sustainable manufacturing practices and the global commitment to achieving Net Zero emissions by 2050, developing more economical and sustainable heat treatment methods has become a critical priority. However, there is currently no systematic comparison between conventional heat treatment methods and emerging alternative techniques in terms of their effects on the alloy's microstructure and mechanical properties. A comprehensive study assessing the effectiveness of rapid heat treatment methods is urgently needed. Additionally, manufacturers require clear guidelines on the optimal settings for novel heating techniques to boost their practical adoption and accelerate their integration into industrial manufacturing.

Motivated by these needs, this work aims to provide a detailed comparison of conventional heating methods, such as electric and gas furnaces, with novel rapid and energy-efficient techniques, including induction coil and infrared heating, for the solid solution treatment of high-strength 7075 aluminium alloy. This study includes a comprehensive characterisation of the material's behaviour, focusing on precipitate distributions, grain structures, and post-heat-treatment hardness, supported by finite element (FE) analysis of the thermal processes. By evaluating the microstructural impact and industrial feasibility of these novel heating methods, this research aims to identify the most suitable and sustainable heating techniques for follow-up hot-working operations, such as forging. The insights gained will facilitate the adoption of alternative heating technologies, contributing to more efficient and environmentally friendly manufacturing practices in the aluminium industry.

2. Materials and Methods

2.1. Heating Methods

All unheated and heated 7075 aluminium billets were supplied with an identical diameter of 60 mm. Six billets were analysed in this study. The billet used as the benchmark as-received sample did not experience any heat treatment. The other five billets were heat-treated from room temperature to a solid solution temperature of 450 °C using conventional (electric furnace and gas furnace) and novel (induction coil, infrared module, and infrared furnace) heating methods. For the gas furnace heating, a David Etchells (furnaces) Ltd. (Birmingham, UK) ZYG32 rotary gas furnace was used. For the electric furnace, an unidentified manufacturer industrial electric furnace at the drop-forging company was used. For the induction coil heating, a Still Induction Heating Ltd. (Droitwich, UK) STS40 induction system was used. For the infrared heating, a full infrared furnace

manufactured by Excelitas Heraeus Noblelight was used in the full infrared furnace heating experiment, and a Heraeus Noblelight (Cambridge, UK) overhead module Z8 8006-2496 HPSW System (S5 Module) was used in the infrared module experiment. Details of the heat treatments, including target temperature, soaking time, and approximate heating rate ranges—calculated via FE methods where possible—are provided in Table 1. After heat treatments, the billets were subjected to subsequent rapid cooling through water quenching to room temperature, followed by natural ageing for around two years, ensuring stable microstructures and properties.

Table 1. Details of the heat treatment conditions of the six groups of samples.

Sample	Heating Methods	Target Temperature, °C	Soaking Time, min	Heating Rate Range, °C·min^{-1}	Specific Energy Consumption, kWh
UH	Unheated	n/a	n/a	n/a	n/a
EF	Electric furnace	450	60	Up to 19	0.11
GF	Gas furnace	450	60	Up to 20	0.15
IC	Induction coil	450	5	95	0.366
IM	Infrared module	450	10	44	0.065
IF	Infrared furnace	450	20	22	0.085

An estimate of the specific energy consumption of each heating method has also been provided, based on quoted furnace machine power and with estimates for the maximum number of samples capable of being heated per run. However, these figures will clearly be rather approximate and vary depending upon the actual furnace equipment used, the physical size of the heating chamber, the size and the number of billets required for heating, and the applied packing arrangement. For instance, a partly empty furnace is less efficient, increasing specific energy consumption per billet. The higher specific energy consumption for induction coil heating is due to its ability to heat only a single billet at a time, compared to multiple billets being heated simultaneously in a furnace batch. However, for a small number of billets, induction coil heating can still be much more time- and energy-efficient than a furnace that is not fully loaded.

2.2. Sample Characterisation

As depicted in Figure 1, all billets were first cut perpendicular to the longitudinal (LD) direction (i.e., extrusion direction) into 10 mm thick cylindrical discs and further cut into 10 mm wide strips along the diameter. Two samples were made by the final cuts. One sample was a $10 \times 10 \times 10$ mm^3 cube from the centre region; the other was from the edge region with five 10×10 mm^2 square faces, and one lateral face retains the original curvature of the cylindrical disc, as shown in Figure 1. The cut cube samples were hot mounted by Bakelite at 180 °C, leaving the surfaces highlighted as red exposed (Figure 1). Mounted samples were water-assisted ground with silicon carbide paper in the order of P400, P800, P1200, and P2400, polished with 6, 3, and 1 µm diamond suspension and 0.06 µm colloidal silica for the final step.

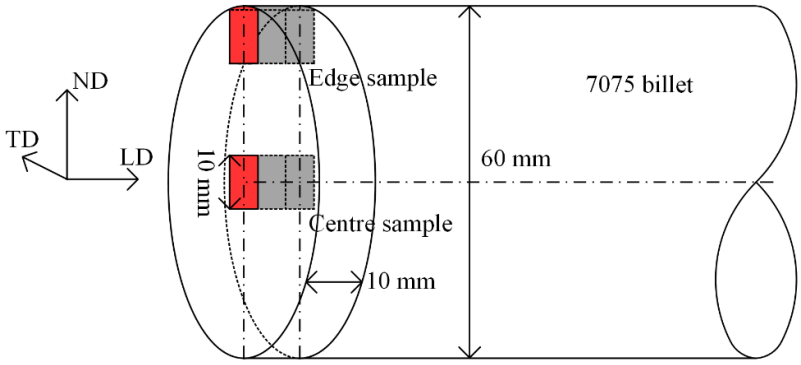

Figure 1. Schematic of the edge and centre samples sectioned from the billet.

Scanning electron microscopy (SEM) images were obtained by a TESCAN MIRA3 electron microscope in backscattered electron (BSE) mode for imaging the precipitates. The accelerating voltage for imaging was selected as 20 keV, and the working distance was kept at 10 mm. The chemical compositions of the second-phase particles were analysed by energy-dispersive X-ray spectroscopic (EDS) scanning. Electron backscattered diffraction (EBSD) scanning was used to investigate the grain sizes and orientations. The sample was placed in a 70° pre-tilt stage. Acceleration voltage and working distance were set to 20 keV and 15 mm, respectively.

Vickers microhardness testing was performed on the polished cross-sections using a Buehler automatic microhardness tester. The applied load was set to 500 g, and the holding time was set for 10 s. As shown in Figure 2, each sample was tested with 20 points along the centre cross with a constant 1 mm spacing and 0.5 mm away from the edge of the surface.

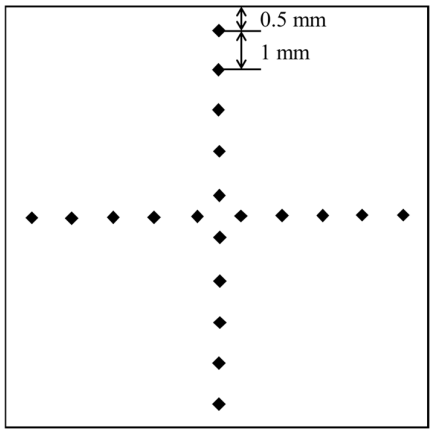

Figure 2. Layout of the hardness testing locations on each sample.

2.3. Heating Simulation

To better understand the thermal loads, the heating rates, and the cooling rates involved with the pre-forging heating process, a finite element framework was created for the representative heating methods examined in this study. The FE models were created using commercial metal forming and heat treatment software DEFORM 2D/3D v11.0, by developers Scientific Forming Technologies Corp. (Columbus, United States). The model was constructed in a 2D axisymmetric condition, with the axis of symmetry aligned to the centre of the cylindrical billet. A representative cylindrical workpiece, measuring 60 mm in diameter by 40 mm high, was created and assigned the relevant thermo-mechanical properties of the aluminium alloy 7075. These properties are illustrated in Table 2.

Table 2. Thermo-mechanical properties of 7075 alloy.

Young's Modulus, GPa	Poisson Ratio	Thermal Expansion, K^{-1}	Thermal Conductivity, $W \cdot m^{-1} \cdot K^{-1}$	Density, $kg \cdot m^{-3}$	Specific Heat Capacity, $J \cdot kg^{-1} \cdot K^{-1}$
68.9	0.3	22×10^{-6}	180	2810	960

The modelling strategy for the heating stage was dependent upon whether the heating operation was a convective heating type approach (gas furnace or electric furnace) or an induction heating method. For standard convective heating, represented by the use of an electric furnace, a simple convective heat transfer model between the workpiece and the heated atmospheric surroundings was constructed. In this case, an associated atmospheric temperature function was programmed using thermal data from experimentally measured furnace temperature. An assumption that the furnace was perfectly uniform was made rather than considering any variation in temperature across the furnace due to seal leakages or heating element location. The target atmospheric temperature was 450 °C. The thermal boundary conditions to accurately describe the heat transfer were a constant heat transfer coefficient of 25–35 $W \cdot m^{-2} \cdot K^{-1}$, which was used to represent the free convection within a simple electric furnace with no forced convection currents present [16]. This was replaced with a value of approximately 60 $W \cdot m^{-2} \cdot K^{-1}$ for the gas furnace.

In the case of induction coil heating, a bespoke induction heating framework was developed, whereby the representative induction coil cross-section, workpiece cross-section, and a meshed workpiece around it all to represent the air were constructed. A considerably finer element size was used at the air-to-workpiece interfaces to capture in greater detail the heat being inducted into the skin of the aluminium billet. For the induction heating model, the air was required to be meshed and assigned a thermal conductivity of 1 $W \cdot m^{-1} \cdot K^{-1}$ and electrical resistivity of 1.3×10^{16} $\Omega \cdot m^{-1}$. Mechanical boundary conditions to apply a floor beneath each billet were applied to prevent motion. A simplistic FE infrared heating model was not feasible as the process does not see heated air convection temperatures at a solid body interface—the air does not get heated during infrared methods. Thus, the multiphysics required are not implemented in the DEFORM FE code. Research has been conducted on infrared heating simulation [17], although it has not been implemented within this work. All meshes and modelling frameworks for the heating models can be seen in Figure 3.

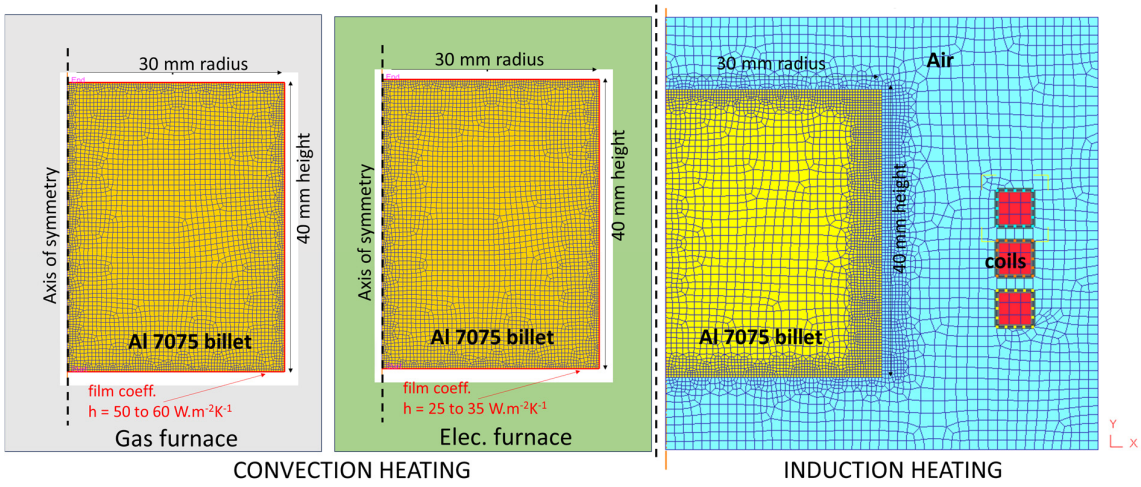

Figure 3. Schematic of 7075 billets heated by convection heating (**left**) and induction heating (**right**).

To model the post-heating quenching operation that occurred experimentally, a similar convective heat transfer model was set up, this time with a heat transfer coefficient with temperature dependence, varying from 1150 $W \cdot m^{-2} \cdot K^{-1}$ at low temperatures, up to 2100 $W \cdot m^{-2} \cdot K^{-1}$ at the sample starting temperature of 450 °C, based upon work in the literature for a different Al alloy, namely 6061 [18].

3. Results and Discussion

3.1. Microstructure Characterisations

Figure 4 illustrates the SEM BSE images captured in the edge (Figure 4a) and centre (Figure 4b) regions of all samples. For simplicity, the abbreviations for the heat treatment types of the samples, as denoted in Table 1, will be used hereinafter. The as-received UH sample exhibits a typical overaged microstructure for the 7xxx series [6,19], characterised by a high density of coarse, medium-sized second-phase particles visible in the high-magnification images of both edge and centre regions.

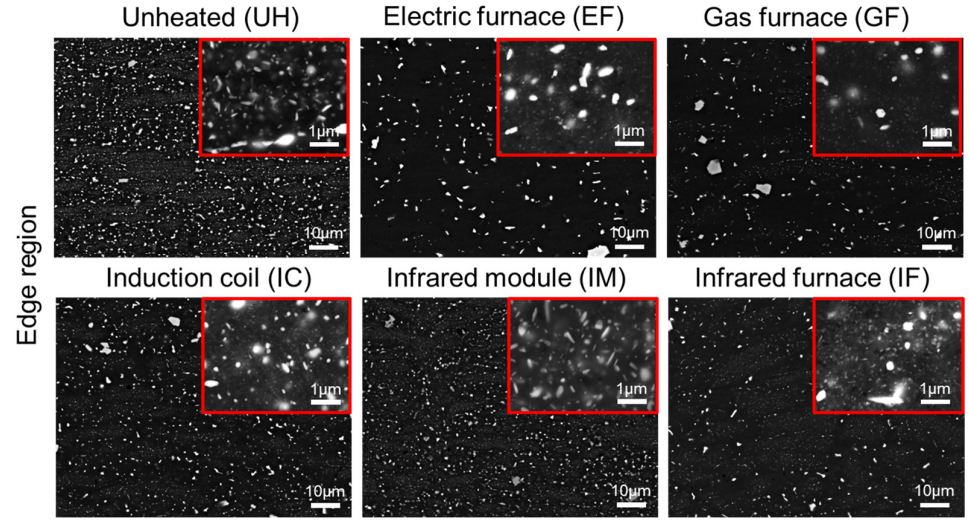

(**a**)

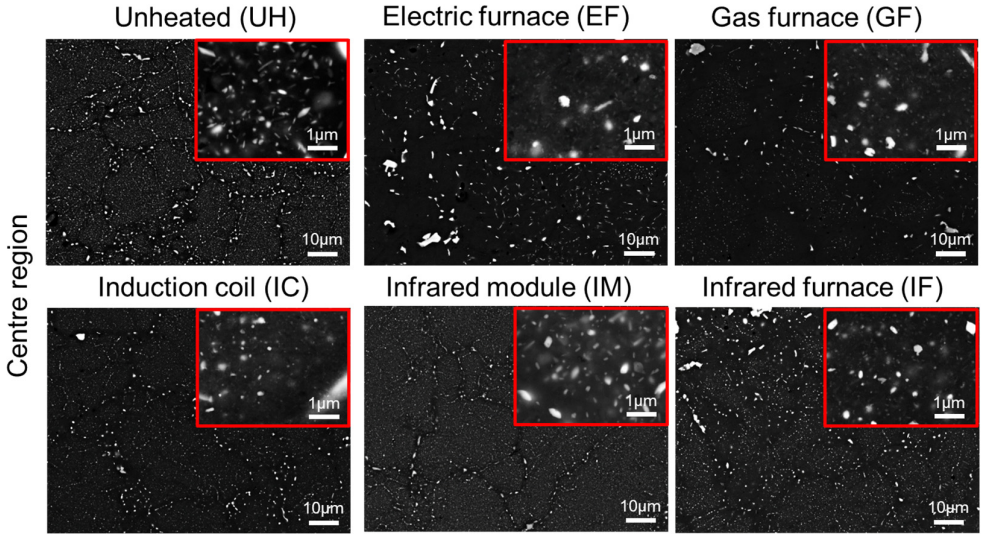

(**b**)

Figure 4. SEM BSE images captured from the (**a**) edge and (**b**) centre regions of all six samples. The images in the top-right red boxes are at a magnification 10 times higher.

The majority of these particles are slightly smaller than 1 μm in size, which is similar to the average size of stable, plate-like, or rod-shaped η phase ($MgZn_2$) seen in other 7xxx series aluminium [10]. In comparison, the conventionally heated samples EF and GF show a distinct microstructure. In these samples, the medium-sized phases observed in the UH sample were mostly dissolved, leaving a small number of large, non-dissolvable particles. This suggests that these conventional solid solution heat treatments applied were satisfactory. It can also be observed from the high-magnification images that a high density of ultrafine particles (less than 0.1 μm) is present between the large particles in the EF and GF samples, which are not visible in the UH sample. For non-conventional heating methods, IC and IF samples have similar microstructure configurations as EF and GF, whereas the IM sample is similar to the UH sample, indicating that the heat treatment was unable to dissolve the stable phases. This was likely due to insufficient heat treatment duration and increased exposure to air, leading to a higher level of heat dissipation.

Figure 5 compares the EDS mapping in the edge regions of the UH sample, which was observed in the overaged condition, and EF samples in which the medium-sized particles were mostly dissolved. One notable distinction observed is that the medium-sized particles in the UH sample were rich in magnesium and zinc contents (as exemplified by the red squares in Figure 5a), in contrast to the EF sample (Figure 5b), where magnesium only existed in the larger, undissolved intermetallic phases, and zinc was undetectable. This observation aligns with the SEM observation, indicating the complete dissolution of the medium-sized η phase ($MgZn_2$) particles. Another study similarly reported the presence of Mg- and Zn-rich particles, which were identified by EDS mapping following the T6 and T73 heat treatments [12]. Consequently, the ultrafine re-precipitated particles in the EF sample remained below the detection threshold of the EDS analysis.

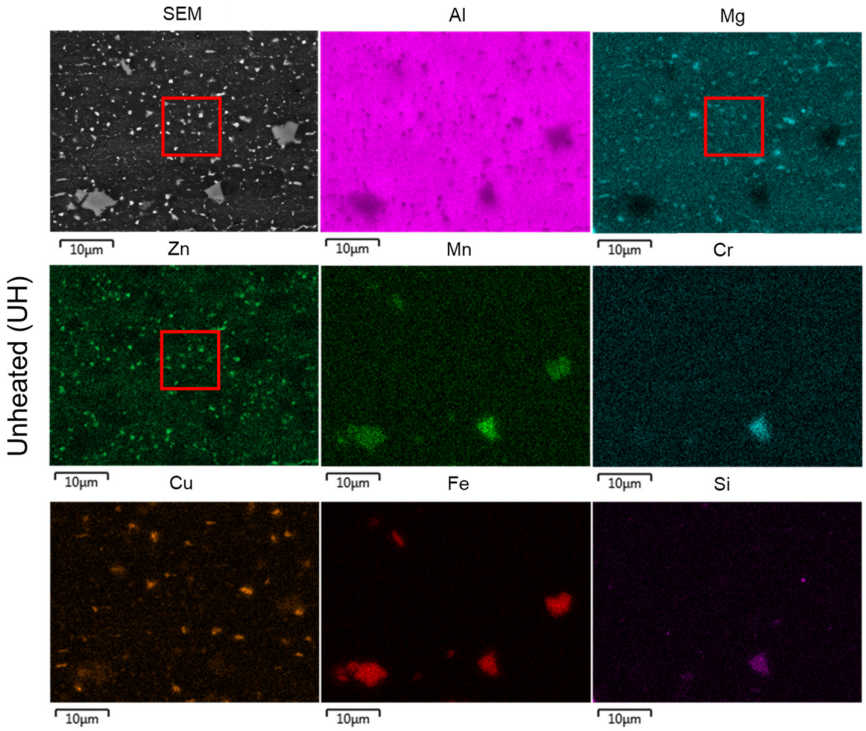

(**a**)

Figure 5. *Cont.*

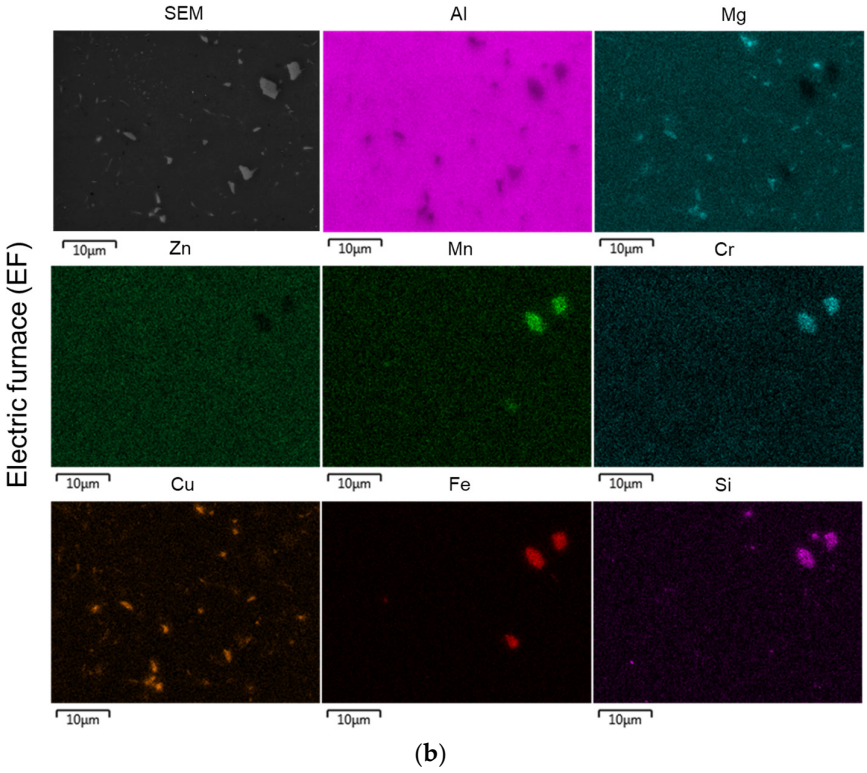

Figure 5. EDS mapping of the major elements present in the second-phase particles of the (**a**) unheated (UH) sample and (**b**) electric furnace (EF) heated sample. Red boxes indicate medium-sized particles which were rich in magnesium and zinc contents.

Additionally, some other large particles present were enriched with manganese, chromium, copper, iron, and silicon. These are likely intermetallic compounds, such as $Al_{12}Si(Fe,Cr)_3$ [8], Al_2CuMg, or Mg_2Si [20], primarily composed of main alloying elements in 7xxx series alloys. They are formed as a result of local chemical composition variations and the solidification rate during casting. These intermetallic compounds can contribute to enhancing strength and toughness, refining grain structure, and mitigating solidification cracking [21].

The EBSD inverse pole figure (IPF) maps of the edge and centre regions with respect to the TD, ND, and RD are presented in Figure 6. In the LD map of the centre region (Figure 6b), the blue and red colours indicate grains predominantly oriented in the <111> and <001> directions, aligning with the original manufacturing route extrusion axis. This is characteristic of a double-fibre texture in extruded aluminium [22], also observed in another study in AA2014 extruded billet [23]. A double-fibre texture is a crystallographic configuration where most grains are oriented along the <111> direction (blue colour), with a smaller fraction along <100> (red colour). This texture is formed due to the deformation (i.e., extrusion of the billet) and recrystallisation processes during the thermomechanical process experienced by the alloy. In contrast, the ND and TD maps show a mix of green (indicative of <101> direction), purple (a mixture of <111> and <001> directions), and red (<001> direction) colours. This varying in orientations suggests that the grains are oriented more randomly in directions perpendicular to the extrusion axis (i.e., along the billet radius), with <101> being a prominent orientation in these directions. On the other hand, no notable differences in size and morphology are observed between the different heat treatment methods.

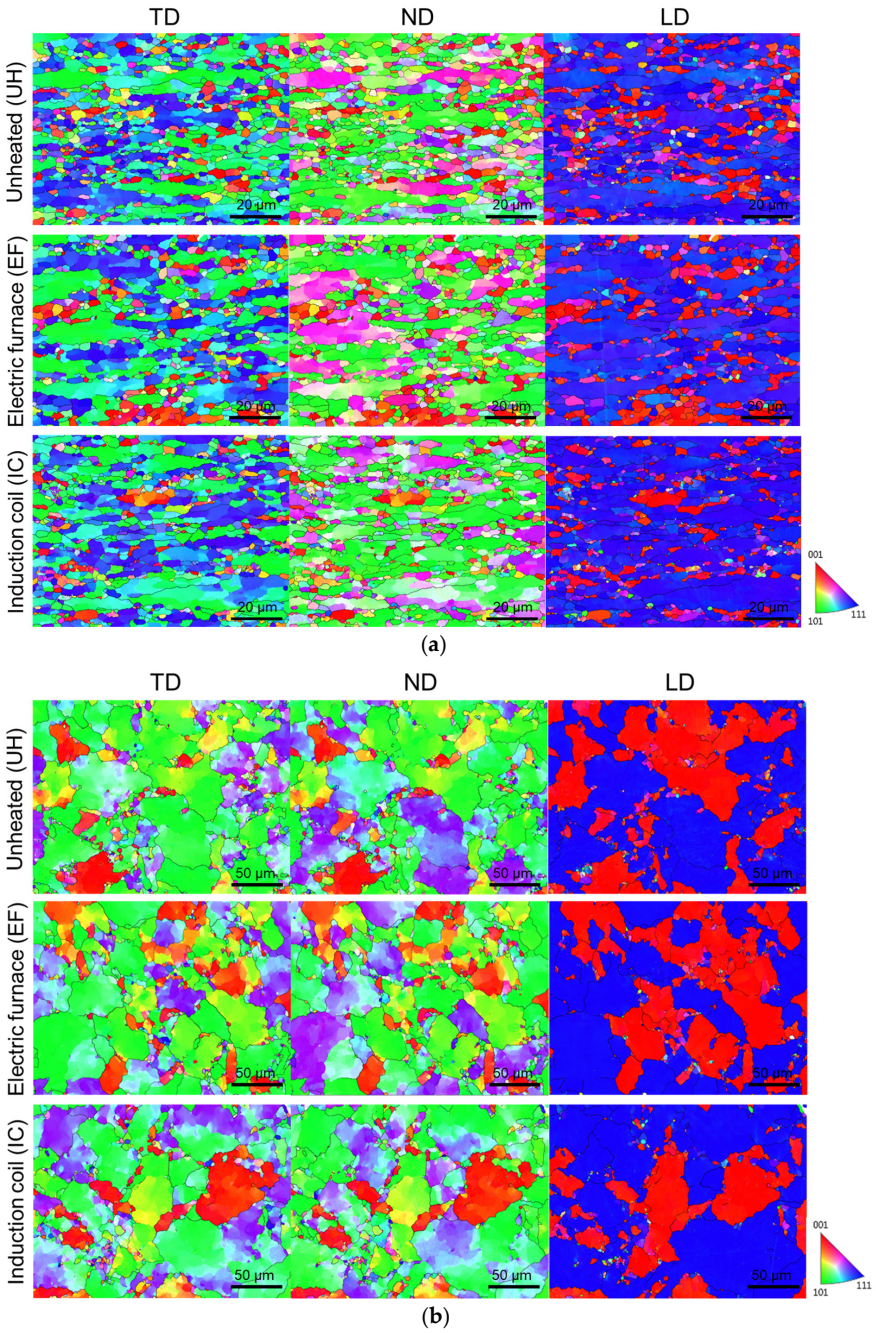

Figure 6. EBSD IPF maps of the grain structures relative to the TD, ND, and LD in the (**a**) edge and (**b**) centre regions of the unheated (UH) sample, compared with samples heat treated using the electric furnace (EF) and the induction coil (IC). Note the difference in the scales.

For the EBSD analysis, the comparisons focus on the most representative methods: the conventional EF method, identified through SEM as achieving complete solution treatment, and the novel IC method, which demonstrated significant dissolution of precipitates under rapid heating conditions. These two methods are compared with the benchmark unheated sample (UH) to evaluate whether the substantial differences in heating rates and hold times between EF and IC result in observable changes in grain structure. For the edge regions (Figure 6a), the higher proportion of blue-coloured <111> grains in the TD map at the edge, compared to the centre, suggests a stronger influence of shear deformation near the billet surface. This is likely due to the friction and shear as the material passes through the original manufacturing route extrusion die, leading to a slightly different texture than in the centre region. The presence of smaller, more elongated recrystallised grains with a

higher aspect ratio at the edge region further supports this, as they indicate more intense deformation compared to the centre region. In contrast, the centre of the billet experiences significantly less shear deformation, resulting in larger grains with lower aspect ratios exhibiting grain morphologies similar to those observed in the 7075 alloys in the as-received condition [3]. Similarly, the grain sizes or morphology sizes in the edge region were not affected by the heat treatments.

The pole figures shown in Figure 7 are in agreement with the EBSD maps, revealing that the centre regions exhibit a strong, characteristic double-fibre texture configuration. In contrast, the edge regions show a weakened double-fibre texture (as indicated by approximately half the intensity scale of the centre region) and slight deformation. This is attributed to the higher shear stresses and strain rates at the edge of the billets during the extrusion process.

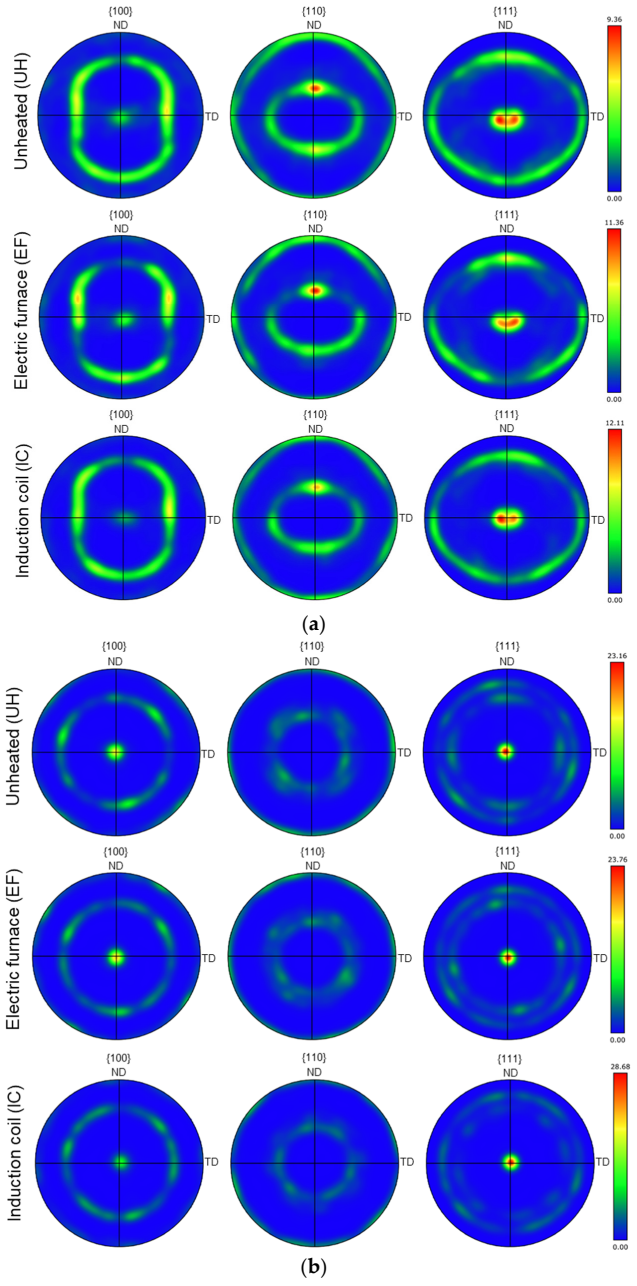

Figure 7. Pole figures of the (**a**) edge and (**b**) centre regions of the unheated sample, compared with samples heat treated using the electric furnace (EF) and the induction coil (IC).

3.2. Hardness Measurements

Figure 8 plots the average hardness values measured in the edge and centre regions of all samples. In general, the samples with dissolved medium-sized precipitates show elevated hardness levels, ranging approximately between 130 and 140 HV. Conversely, samples in the overaged condition, i.e., UH and IM, demonstrate remarkably lower hardness, around 70 HV. Notably, for all samples, there is a uniform hardness distribution between edge and centre regions. An inverse correlation is evident between the proportion of second-phase particles (quantified from 5x SEM micrographs) and the hardness values. This is consistent with the finding from the SEM micrographs (Figure 5), as the medium-sized stable η phase in overaged samples like UH and IM contributes less to strengthening due to the inefficient bowing reaction between particles and dislocations. In contrast, the dissolution of medium-sized particles during solution heat treatment elevates the solute atom concentration in the solid solution. Subsequent natural ageing precipitates dense, ultrafine metastable phases (GP zones and η'), significantly enhancing the strength [24,25]. This mechanism explains the noticeable increase in hardness observed in IC, IF, EF, and GF samples. This phenomenon also mirrors the findings from a similar study conducted on the 2014 alloy [23].

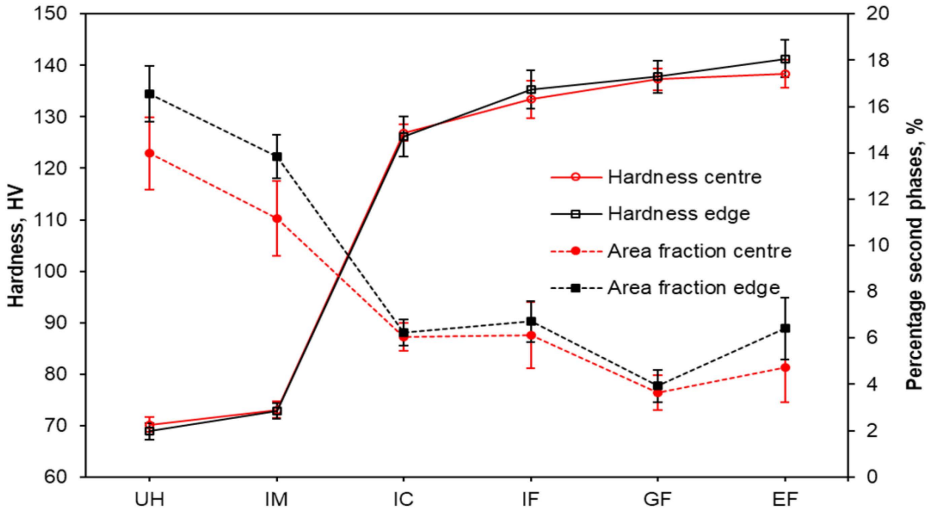

Figure 8. Comparison of the Vickers hardness and the percentage of the second phase particles in the edge and centre regions of all samples. Error bars represent standard errors. UH, IM, IC, IF, GF, and EF denote the unheated sample and samples heated by an induction coil, infra-red module, infra-red furnace, gas furnace, and electric furnace, respectively.

The average grain sizes of the UH, IC, and EF samples, as depicted in Figure 9, were calculated using the data obtained from the EBSD maps provided in Figure 6. These sizes align with the visual assessments that the edge regions and centre regions are around 3 and 8 μm, respectively. Notably, despite these large variations in grain size, the hardness values of both edge and centre regions for a given sample are at the same level, indicating their independence from grain size. This observation further supports the conclusion that hardness in these samples is primarily impacted by the state of the precipitates rather than the average grain size.

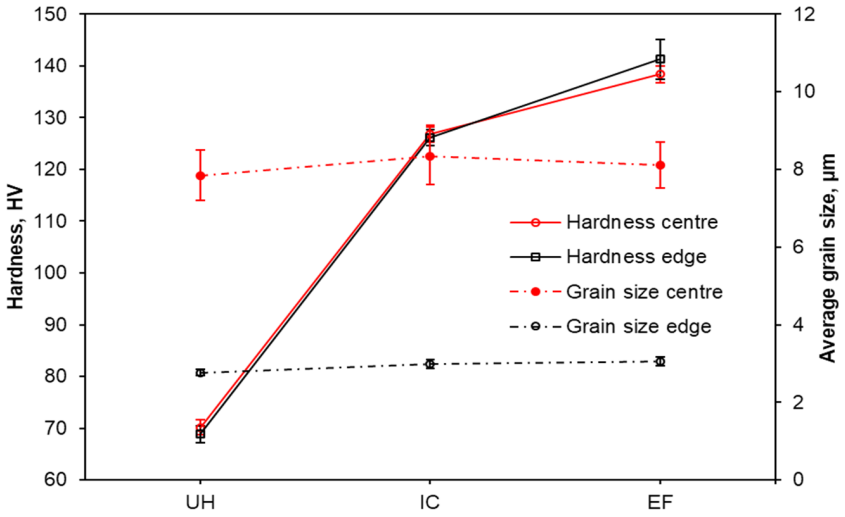

Figure 9. Comparison of the Vickers hardness and the average grain size in the edge and centre regions of all samples. Error bars represent standard errors. UH, IC, and EF denote the unheated sample and samples heated by an induction coil and electric furnace, respectively.

3.3. Simulation Results

Due to the high thermal conductivity of 7075 aluminium alloy and small billet size, there were only very minor temperature differences predicted by FE between the centre and the edge of the billet during the heating process for all types of heating methods, as shown in Figure 10. For the induction coil (IC) model, the centre was typically cooler than the edge by up to 5 °C, as shown in Figure 10. Note that in the IC model, the operator cannot allow the sample to soak at the target temperature for a period of time. Once the outer edge is measured at 450 °C by the thermocouple probe kit, reaching the target temperature, the power is cut to the induction unit. This means that when the power to the induction unit is cut, the central region of the IC billet is predicted to be roughly 5 °C cooler than the target soaking temperature, and the centre is unlikely to ever reach the target temperature.

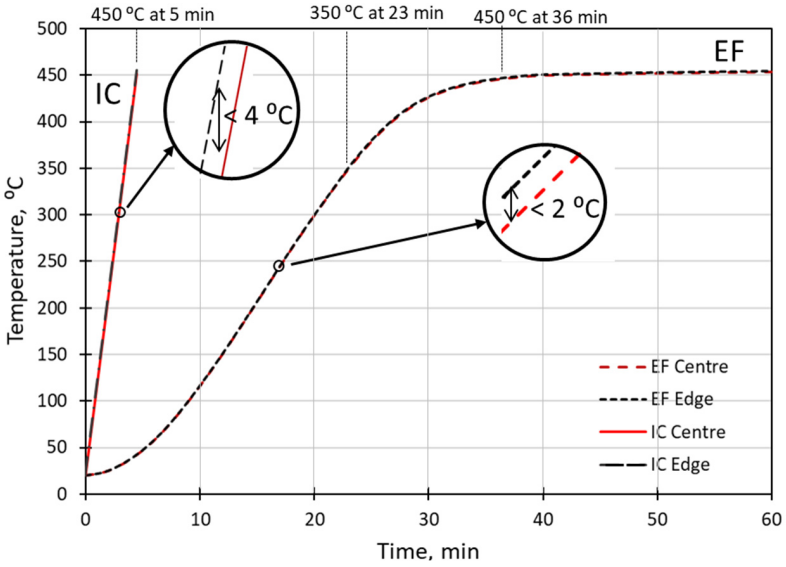

Figure 10. Predicted temperatures at the centre and the edge of the billet during the heating process for the electric furnace (EF) and induction coil (IC) heating methods.

For the electric furnace (EF) model, the centre of the 7075 billets was typically up to 2 °C cooler than the edge. In this model, the 7075 billet took 36 min to reach approximately

a uniform target temperature of 450 °C, although after only 23 min it had already reached 350 °C. The EF sample increased in temperature much more quickly when there was a larger thermal difference between the aluminium billet and the hot atmosphere. This changing instantaneous heating rate for the electric furnace (EF) sample, ranging up to roughly 19 °C/min, is reflected in Figure 11a, compared to the relatively steady and significantly higher heating rate of the induction coil (IC) sample, of roughly 90–95 °C/min (Figure 11b).

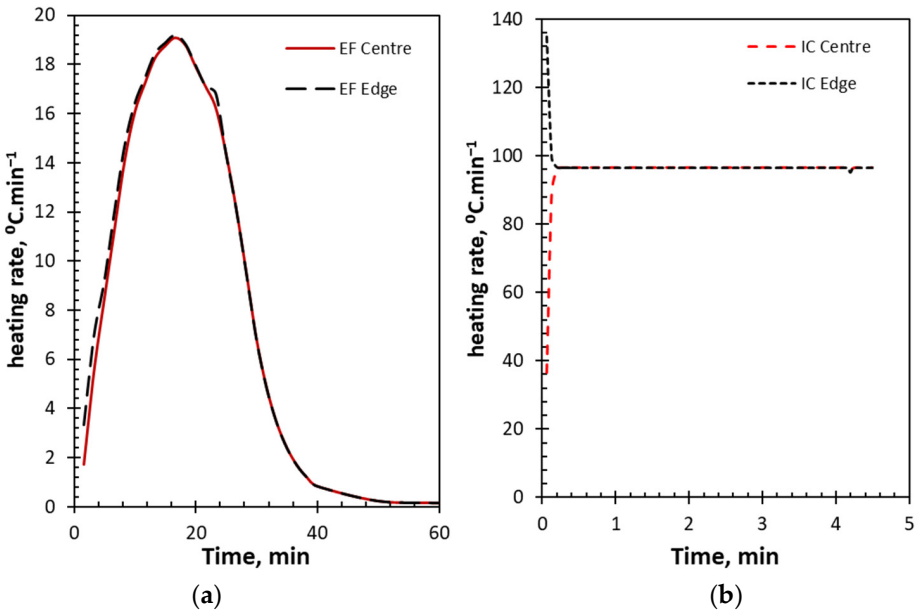

Figure 11. Predicted heating rates at the centre and the edge of the billet during the heating process for (**a**) electric furnace (EF) and (**b**) induction coil (IC) heating methods.

In the FE model, no transfer time or changing thermal convection coefficient to represent the sample being moved through the air from the furnace to the quench tank was considered. The last thermal profile from the heating phase was simply passed into the quenching model to be the starting condition for the quench. During the quenching operation, predictably, all the different heating methods used display virtually identical cooling rates for a given location within the billet, as these cooling rates are purely a function of the starting temperature and the heat transfer during the quenching operation; see Figure 12. The preceding heating operation to obtain the samples up to the target 450 °C was considered largely immaterial as they all reached the approximately uniform target temperature, within 5 °C.

Upon closer analysis of the thermal predictions in Figure 12, a variation in the thermal load experienced by the centre and outer edges of the billet becomes more apparent during quenching, with the edges cooling considerably faster than the centre. During the early stages of the quench, the edge of the sample was up to 50 °C cooler than the hotter centre, resulting in a parabolic thermal gradient across the radius of the billet. The maximum temperature gradient, approximately 4° C·mm^{-1}, was predicted at the outer edge and observed very early in the quench operation, within the first second or so.

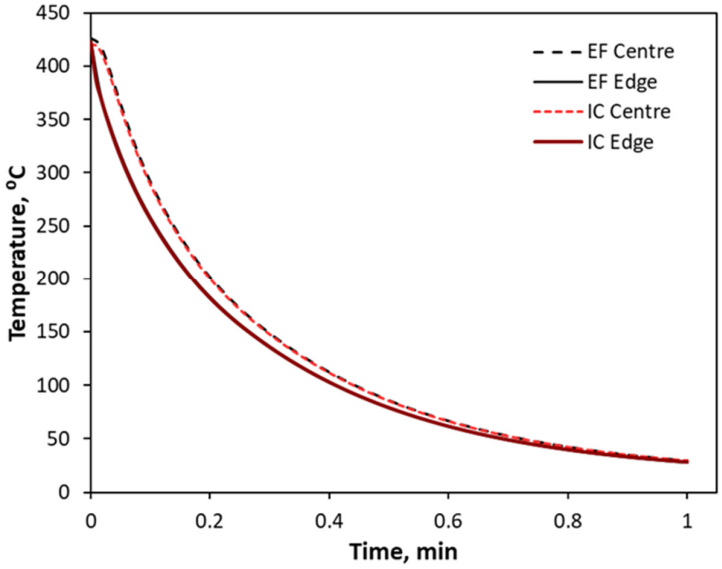

Figure 12. Modelled cooling curves from solution temperature to room temperature for the electric furnace (EF) and induction coil (IC) heating methods.

The instantaneous cooling rates were computed by differentiating the temperature versus time curves during the quench, as shown in Figure 13. The peak cooling rate at the outer edge was approximately 70 °C·s^{-1}, occurring at the very start of the quench. In contrast, the peak cooling rate at the centre of the billet was significantly lower, at only 29 °C·s^{-1}, occurring approximately several seconds into the quench.

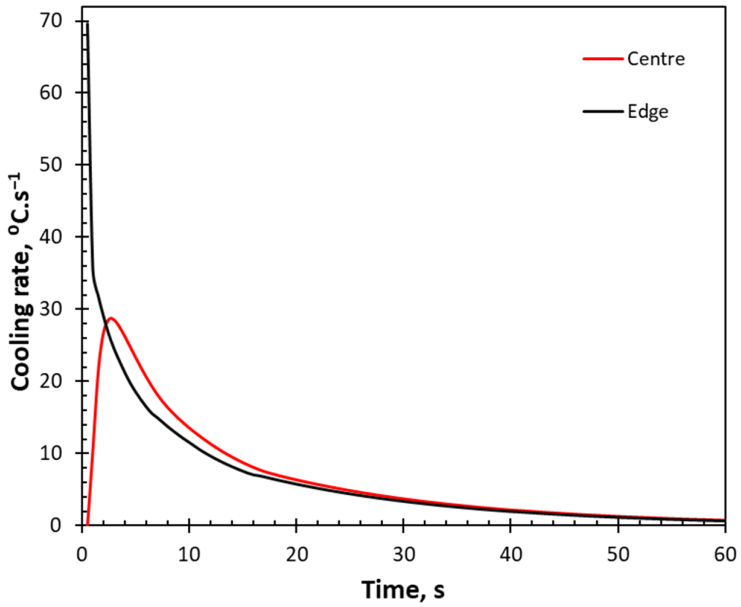

Figure 13. Predicted cooling rates for the edge and centre regions within the billet.

Despite these differences in cooling rates between the edge and centre regions, experimental results have shown that the supersaturated solid solution formed in the effectively solution-treated samples (EF, GF, IC, and IM) was uniformly retained across both regions after water quenching. This was evidenced by the similar states of precipitates observed between the edge and centre. Hence, the differential cooling rates appear to have a negligible impact on the microstructural configuration in this context. This observation confirms the effectiveness of rapid quenching in stabilising the supersaturated solid solution, enabling the subsequent reprecipitation of the ultrafine strengthening phase.

Due to the relatively large gap between the solidus and liquidus temperatures of 7075 alloy, it is feasible and "safe" to slightly exceed the solution treatment temperature without the risk of incipient melting. Additionally, the experimental observations in this study indicated that the dissolution of precipitate phases occurs rapidly upon reaching the solution temperature. This finding aligns with Liu et al.'s findings [11], which demonstrated that extending the soaking time from 10 to 70 min at solution temperature results in negligible changes in hardness, suggesting that prolonged soaking provides minimal additional benefit once the solution treatment is complete.

Furthermore, induction coil heating is particularly well-suited for solution treatment of 7075 alloys. Its ability to provide uniform and rapid heating significantly reduces the time required for heat conduction throughout the billet, ensuring efficient and consistent treatment. This is particularly advantageous in this study, as the billet's cylindrical shape optimises the effectiveness of induction coil heating, further supporting its suitability.

4. Conclusions

This study aimed to demonstrate the superiority of innovative, rapid, cost- and energy-efficient heating methods that can be potentially adopted as alternatives to conventional heating methods, namely induction coils, infrared modules, and infrared furnaces, over conventional methods like electric and gas furnaces in the solid solution treatment of 7075 aluminium alloy. To this end, five identical 7075 alloy billets of 58 mm diameter underwent heat treatment using the aforementioned methods, and their properties were compared to an untreated benchmark billet. The comparison involved detailed microstructure investigations through SEM (for precipitate distribution), EBSD (for grain structure), and Vickers microhardness testing, supplemented by FE modelling to compare the heating and cooling processes of conventional (electric furnace) and novel (induction coil) methods.

The SEM images indicate that the as-received benchmark UH sample is in an overaged condition, characterised by a dense distribution of medium-sized (~50 nm) second-phase particles, presumed to be the stable η phase, along with larger, non-dissolvable intermetallic phases. This is supported by EDS mapping, which shows that in EF and GF samples, most of the medium-sized particles rich in Mg and Zn have dissolved after thorough solution treatment, in contrast to the UH sample. In the EF and GF samples, a high density of ultrafine particles is uniformly distributed among the larger intermetallic phases. These ultrafine particles are likely GP zones and η' phases formed during subsequent natural ageing. The IC and IF samples exhibit similar microstructural configurations. In contrast, the precipitate distribution of the IM sample resembles the UH sample, indicating incomplete dissolution of the stable η phase particles.

The EBSD IPF maps indicated distinct texture differences between the edge and centre regions of the UH, EF, and IC samples. The centre regions displayed a double-fibre texture as a response to extrusion, with grains predominantly oriented in <111> and <001> directions. However, the edge regions exhibited a more varied orientation compared to the centre regions, with a prominent <101> orientation (relative to the TD), indicating more random grain alignment due to shear deformation from the extrusion die. These findings were further confirmed by pole figure analyses. No notable differences in grain structures or textures were altered by the heat treatments.

Hardness results showed that the EF and GF achieved hardness ranging from 137 to 141 HV, compared to the UH sample of approximately 70 HV. The IC and IF demonstrated effectiveness with similar hardness between 126 and 135 HV. The average grain sizes determined by EBSD in centre and edge regions for all samples were 3 and 8 μm, respectively. However, the impact of the grain size on the hardness is negligible, suggesting the hardness is dictated by the precipitate distribution.

FE modelling comparing the EF and IC heating processes showed that the IC could heat the billet to 450 °C ten times faster than the electric furnace. The model also suggested variances in cooling rates upon water quenching between edge and centre regions. However, the microstructure and microhardness results have demonstrated that in the effectively solution-heated samples (EF, GF, IC, and IF), the supersaturated solid solutions were uniformly achieved across both edge and centre regions, implying that the different cooling rates appear to have a negligible influence.

This study highlights the efficiency of novel heating methods, particularly induction coil heating, in significantly reducing the duration required for solution heat treatment to achieve the pre-forging condition of 7075 aluminium alloy. These methods demonstrate considerable potential to accelerate heat treatment processes while maintaining the desired level of solution treatment and achieving comparable post-treatment material properties, thereby making the process more economical and sustainable. Further refinement of heating times is recommended to improve the efficiency and consistency of the process. Additionally, a comprehensive assessment of the mechanical performance of the treated materials is necessary to validate their suitability for industrial applications.

Author Contributions: Conceptualisation, H.W., S.H. and R.T.; data curation, H.W., Z.L. and S.H.; formal analysis, H.W., Z.L. and R.T.; funding acquisition, R.T.; investigation, H.W., Z.L. and R.T.; methodology, H.W., S.H. and R.T.; resources, S.H.; supervision, H.W. and R.T.; visualisation, H.W., Z.L. and R.T.; writing—original draft preparation, H.W., Z.L. and R.T.; writing—review and editing, H.W., Z.L., S.H. and R.T. All authors have read and agreed to the published version of the manuscript.

Funding: This research received no external funding.

Data Availability Statement: The data presented in this study are available on request from the corresponding author due to commercially sensitive proprietary information.

Acknowledgments: The authors offer thanks to WH Tildesley Ltd., Willenhall, UK, for the materials and the heating trials. Thanks are offered to Yu-Lung Chiu at the Facility for Electron Microscopy, School of Metallurgy and Materials, University of Birmingham, for the use of the microscopy characterisation equipment. Thanks to Ian Bartley at Excelitas for support with the Noblelight IR heating trials and for energy consumption data for these units.

Conflicts of Interest: Author Steven Hill was employed by WH Tildesley Ltd. The remaining authors declare that the research was conducted in the absence of any commercial or financial relationships that could be construed as a potential conflict of interest.

References

1. Polmear, I.; St. John, D.; Nie, J.F.; Qian, M. *Light Alloys: Metallurgy of the Light Metals*; Elsevier: Amsterdam, The Netherlands, 2017.
2. Sha, G.; Cerezo, A. Early-stage precipitation in Al-Zn-Mg-Cu alloy (7050). *Acta Mater.* **2004**, *52*, 4503–4516. [CrossRef]
3. Ghosh, A.; Ghosh, M.; Shankar, G. On the role of precipitates in controlling microstructure and mechanical properties of Ag and Sn added 7075 alloys during artificial ageing. *Mater. Sci. Eng.* **2018**, *A*, 738. [CrossRef]
4. Ghosh, A.; Das, K.; Eivani, A.R.; Mohammadi, H.; Vafaeenezhad, H.; Murmu, U.K.; Jafarian, H.R.; Ghosh, M. Development of mechanical properties and microstructure for Al–Zn–Mg–Cu alloys through ECAP after optimizing the outer corner angles through FE modelling. *Arch. Civ. Mech. Eng.* **2023**, *23*, 78. [CrossRef]
5. Yang, W.; Ji, S.; Wang, M.; Li, Z. Precipitation behaviour of Al-Zn-Mg-Cu alloy and diffraction analysis from η′ precipitates in four variants. *J. Alloys Compd.* **2014**, *616*, 493–500. [CrossRef]
6. Liu, S.; Hou, H.; Shao, W.; Yang, J.; Wang, Z.; Yang, Q.; Llorca, J. Revisiting the precipitation mechanisms of Guinier-Preston zones, η′, and η precipitates in Al-Zn-Mg alloys. *Acta Mater.* **2024**, *268*, 119789. [CrossRef]
7. Chang, Y.L.; Hung, F.Y.; Lui, T.S. A new infrared heat treatment on hot forging 7075 aluminum alloy: Microstructure and mechanical properties. *Materials* **2020**, *13*, 1177. [CrossRef] [PubMed]
8. Chayong, S.; Atkinson, H.V.; Kapranos, P. Multistep induction heating regimes for thixoforming 7075 aluminium alloy. *Mater. Sci. Technol.* **2004**, *20*, 194–202. [CrossRef]

9. Huo, W.; Sun, T.; Hou, L.; Zhang, W.; Zhang, Y.; Zhang, J. Effect of heating rate during solution treatment on microstructure, mechanical property and corrosion resistance of high-strength AA 7075 alloy. *Mater. Charact.* **2020**, *162*, 110535. [CrossRef]
10. Rometsch, P.A.; Zhang, Y.; Knight, S. Heat treatment of 7xxx series aluminium alloys—Some recent developments. *Trans. Nonferrous Met. Soc. China* **2014**, *24*, 2003–2017. [CrossRef]
11. Liu, Q.; Chen, S.; Gu, R.; Wang, W.; Wei, X. Effect of Heat Treatment Conditions on Mechanical Properties and Precipitates in Sheet Metal Hot Stamping of 7075 Aluminum Alloy. *J. Mater. Eng. Perform.* **2018**, *27*, 5765–5774. [CrossRef]
12. Lee, M.S.; Jin, C.K. Investigation of optimal solid solution heat treatment temperature and artificial aging time of Al7075 sheet. *J. Mech. Sci. Technol.* **2022**, *36*, 517–527. [CrossRef]
13. Wu, H. *Systematic Analysis of the Advantages of Stationary Shoulder Friction Stir Welding in Joining High Strength Aluminium Alloy AA7050-T7651*; The University of Manchester: Manchester, UK, 2017.
14. Zhang, P.; Liu, J.; Gao, Y.; Liu, Z.; Mai, Q. Effect of heat treatment process on the micro machinability of 7075 aluminum alloy. *Vacuum* **2023**, *206*, 111574. [CrossRef]
15. Scharf, S.; Bergedieck, N.; Riedel, E.; Richter, H.; Stein, N. Unlocking sustainability potentials in heat treatment processes. *Sustainability* **2020**, *12*, 6457. [CrossRef]
16. Kosky, P.; Balmer, R.; Keat, W.; Wise, G. *Exploring Engineering: An Introduction to Engineering and Design*; Elsevier: Amsterdam, The Netherlands, 2020. [CrossRef]
17. Oh, S.H.; Lee, E.H. A New Approach to Modeling Focused Infrared Heating Based on Quantum Mechanical Formulations. *Appl. Sci.* **2022**, *12*, 3256. [CrossRef]
18. Fontecchio, M.; Maniruzzaman, M.; Sisson, R.D. *Quench Factor Analysis and Heat Transfer Coefficient Calculations for 6061 Aluminum Alloy Probes Quenched in Distilled Water*; Worcester Polytechnic Institute (WPI): Worcester, MA, USA, 2002.
19. Azarniya, A.; Taheri, A.K.; Taheri, K.K. Recent advances in ageing of 7xxx series aluminum alloys: A physical metallurgy perspective. *J. Alloys Compd.* **2019**, *783*, 114–137. [CrossRef]
20. Ghosh, A.; Ghosh, M.; Kalsar, R. Influence of homogenisation time on evolution of eutectic phases, dispersoid behaviour and crystallographic texture for Al–Zn–Mg–Cu–Ag alloy. *J. Alloys Compd.* **2019**, *802*, 276–289. [CrossRef]
21. de Souza, S.H.; Padilha, A.F.; Kliauga, A.M. Softening Behavior during Annealing of Overaged and Cold-rolled Aluminum Alloy 7075. *Mater. Res.* **2019**, *22*, e20180666. [CrossRef]
22. Zhao, Y.; Ma, X.; Chen, H.; Zhao, X.; Liu, X. Preferred orientation and interfacial structure in extruded nano-Al3BC/6061 Al. *Mater. Des.* **2017**, *127*, 148–156. [CrossRef]
23. Turner, R.; Turner, W.; Wu, H. On the Pre-Forging Heating Methods for AA2014 Alloy. *World J. Eng. Technol.* **2023**, *11*, 250–259. [CrossRef]
24. Su, J.Q.; Nelson, T.W.; Mishra, R.; Mahoney, M. Microstructural investigation of friction stir welded 7050-T651 aluminium. *Acta Mater.* **2003**, *51*, 713–729. [CrossRef]
25. Bousquet, E.; Poulon-Quintin, A.; Puiggali, M.; Devos, O.; Touzet, M. Relationship between microstructure, microhardness and corrosion sensitivity of an AA 2024-T3 friction stir welded joint. *Corros. Sci.* **2011**, *53*, 3026–3036. [CrossRef]